Doc. # 9950-1381

IMAGE INVERSION ANALYSIS OF THE HST OTA

(HUBBLE SPACE TELESCOPE OPTICAL TELESCOPE ASSEMBLY)

JPL Contract No. 958888, TRW S/N 57661

TECHNICAL FINAL REPORT

Phase A

M. M. Litvak, March 15, 1991
revised: July 18,1991

This work was performed for the Jet Propulsion Laboratory, California Institute of Technology, sponsored by the National Aeronautics and Space Administration.

Prepared for:
Jet Propulsion Laboratory
California Institute of Technology
4800 Oak Grove Drive
Pasadena CA 91109

Prepared by:
TRW Applied Technology Division
Space and Technology Group
One Space Park
Redondo Beach CA 90278-1001

NOTED
JFM 3-18-92
LPS also reviewed
NO ITEMS

IMAGE INVERSION ANALYSIS OF THE HST OTA

JPL Proposed Contract No. 958888, TRW S/N 57661

TECHNICAL FINAL REPORT Phase A

M. M. Litvak, March 15, 1991

Abstract

Technical work during September-December 1990 consisted of 1) analyzing HST point source images obtained from JPL, 2) retrieving phase information from the images by a direct (noniterative) technique, and 3) characterizing the wavefront aberration due to errors in the Hubble Space Telescope (HST) mirrors, in a preliminary manner. This work was in support of JPL design of compensating optics for the next generation wide-field planetary camera on HST. This digital technique for phase retrieval from pairs of defocused images, is based on the energy transport equation between these image planes. In addition, an end-to-end wave optics routine, based on the JPL Code V prescription of the unaberrated HST and WFPC, was derived for output of the reference phase front when mirror error is absent. Also, the Roddier routine unwrapped the retrieved phase by inserting the required jumps of $\pm 2\pi$ radians for the sake of smoothness. A least-squares fitting routine, insensitive to phase unwrapping, but nonlinear, was used to obtain estimates of the Zernike polynomial coefficients that describe the aberration. The phase results were close to, but higher than, the expected error in conic constant of the primary mirror suggested by the fossil evidence. The analysis of aberration contributed by the camera itself could be responsible for the small discrepancy, but was not verified by analysis. The wavefront Zernike coefficient Z_{11} (in HST OTA Handbook convention) was found to be -0.27 and -0.28 μm for the H1-I1 (HARP 1A data)and O1-P1 (HARP 1B data) pairs of images, respectively. The standard deviation error in these quantities was approximately ± 0.005, due to the iterations with the nonlinear fitting routine for Zernike coefficients. The implied conic constant for the primary mirror was -1.0141 and -1.0146 ± 0.0002 compared to the design value of -1.0022985.

New Technology. No new technology was identified.

IMAGE INVERSION ANALYSIS OF THE HST OTA

TECHNICAL FINAL REPORT Phase A

TABLE OF CONTENTS

1.0 Introduction

The Hubble Space Telescope (HST) has not performed as well as designed owing to an imperfect mirror (or mirrors). The Jet Propulsion Laboratory (JPL) is to define the mirror imperfections and to plan a hardware fix in their Wide Field Planetary Camera (WF/PC) to compensate for the aberrations. The work reported here supported JPL in defining the HST aberration by means of a direct phase retrieval technique. This technique operated on digital images of stars to obtain the shape of the optical wavefront in the exit pupil plane. This wavefront distortion was defined in classical terms such as spherical aberration, coma, astigmatism, and so on. This wavefront analysis also would lead to a Code V prescription, for example, of optical elements of the WF/PC that would be needed to compensate for the aberrations.

Early on, it was recognized that spherical aberration was present in large amounts. This led to the suspicion of an incorrect conic constant, which specifies the hyperboloid shape of the primary mirror. The purpose of the phase retrieval work was to quantify this suspicion, and to determine if other errors existed in the primary mirror, other errors might be in the secondary mirror and the camera. A strategy of using multiple off-axis images for distinguishing secondary from primary mirror errors was voiced by various participants at the first HARP Image Inversion Workshop. To date little work toward this end has been done due to a lack of images at sufficiently large field angles.

The imperfections in the camera might be another story. There is a difference in conic constant error estimates from the fossil evidence (interferograms and notebooks at Perkin-Elmer, now Hughes Danbury Optical Systems), and from the Zernike polynomial coefficient in the phase retrieval effort. This, albeit small, difference of conic constant might be attributed to the camera. End-to-end modeling that includes the camera, with its distinguishing obscurations, has been part of the phase retrieval effort.

Much of the phase retrieval work by others consisted of 1) least-squares fitting of images generated by OTA-camera models with image data, 2) iterative automatic fitting by repeated single or double Fourier transforming between pairs or triplets of image planes and their corresponding pupil planes, and 3) neural network Zernike polynomial output after training with simulated images of known Zernike polynomial input. The work reported here was a direct (noniterative) phase retrieval technique that solves a nonlinear differential equation to complete the field information in the image plane so that a Fourier transform retrieves the pupil plane phase that was sought.

According to PC data, the Airy disk of the point spread function (PSF) would cover a few pixels if the OTA operated as designed. The present condition seemed to result in a peak nearly as sharp but with significant intensity in rings and spokes around the peak.

2.0 Technical Purpose

The work consisted of the following three technical tasks for defining the Hubble Space Telescope (HST) aberration by means of the direct (noniterative) phase retrieval technique developed at TRW. This technique was based on the Gonsalves 'phase diversity' algorithm, which processed pairs of images that differed by a small amount of defocus.

2.1 Task 1. Analysis of JPL Star Images

Digital images were input to the phase retrieval code. The code was modified as follows: 1) to read-in the image data, 2) to define a limited field of view containing each star image, and 3) to register (align) the focus/defocus image pairs.

Simulation of the image intensity distribution for these different cases of wavelength filter and secondary mirror positions was done for two purposes: 1) to allow tests of the phase retrieval algorithm for known amounts of aberration and 2) to enable interpolation between pixels of data for more accurate phase retrieval.

Only cases of star objects lying on axis were analyzed.

2.2 Task 2. Implementation of phase retrieval code

Wave optics of the HST optical train was simulated, as needed for phase retrieval purposes. The code was modified 1) for the effects of apertures, obscurations, etc., and 2) for the mirror displacement aberrations. The phase retrieval code was executed on a VAX 8650 system and a 386-PC (25 MHz, 16 Mbytes RAM) 1) to produce Zernike polynomial fits to the wavefront, and 2) to estimate error limits on the phase retrieval accuracy.

2.3 Task 3. Derivation of preliminary wavefront characteristics

Seidel or Zernike polynomial contributions were estimated after the polynomial-fit routine was integrated into the code. Contour maps of the pupil-plane phase were used to clarify the results. Errors in the wavefront reconstruction by phase retrieval were estimated. Preliminary conclusions were drawn on the conic constant error of the OTA primary mirror.

3.0 Technical Approach

A direct (noniterative) technique for retrieving the phase distortion in the optics of instruments such as the Hubble telescope has been developed, and was used with Hubble telescope data. This technique took the digital information from distorted images of a star at two or more focus settings fairly close together; for example, at center focus and at ,say, half the depth of focus. The requirement was to obtain the local rate of change of the intensity at each pixel with respect to the amount of defocus, in each wavelength band. The more accurate this estimate was, despite noise in the image (including quantization noise due to limited numbers of bits per pixel), the more accurate was the phase map that would be generated.

A simple partial differential equation (based on R. A. Gonsalves' work on 'phase diversity'), using this intensity data, was solved for the phase associated with the aberrated image. The complex field in the image plane was then Fourier transformed to obtain the complex field in a pupil plane. Fresnel wave optics propagation to any other pupil plane was done easily, when needed. The phase of this transform field was displayed then as a contour map to visualize the aberrations This phase was analyzed in terms of the usual polynomials like spherical aberration, astigmatism, and coma for convenient analytic characterization.

This was the stage of work (Phase A) that identified the nature of the aberration for hardware fixes to the instruments (JPL's WF/PC, for example) in order to compensate for the phase error in the telescope optics. Note that amplitude correction as well as this phase correction also could be applied at the pupil plane. Phase retrieval in each wavelength band should be consistent with the same optical path difference owing to the surface figure error of primary and/or secondary mirrors. With the proper variety of PSF's obtained with the WF/PC and the Faint Object Camera, with differing angular offsets, the retrieved phase maps could reveal the analytic form of the surface figure for the primary and secondary mirror, a necessary first step in the optical redesign task for the cameras.

The following is a description of the direct phase retrieval method that utilizes the photon energy transport equation. This equation is applied in the vicinity of the image plane (near paraxial focus) but the equation is applicable at any general position.

3.1 Direct Phase Retrieval Method

FOURIER RELATIONSHIP BETWEEN PUPIL AND IMAGE PLANES

Consider the simple geometry of a pupil plane on one side and an image plane on the other side of the lens equivalent of the telescope and camera system. F is the effective focal length. The wavevector magnitude is

$$k = \frac{2\pi}{\lambda} \tag{3.1}$$

The image plane field h(x,y) is obtained from an integral solution of the Fresnel wave equation, when the pupil plane field H(u,v) is given.

$$h(x,y) \cong -i\lambda F \exp[ik(x^2+y^2)/2F)]$$

$$\int du \int dv \exp[-2\pi iB(u^2+v^2)]\exp[-2\pi i(ux+vy)]H(u,v) \tag{3.2}$$

where the spatial frequency components u, v are

$$u = X/\lambda F \qquad v = Y/\lambda F$$

and X, Y are the coordinates in the pupil plane. Because of the integration over u and v instead of X and Y, the coefficient in the expression for h(x,y) is $-i\lambda F$ instead of the well-known $-i/(\lambda F)$. The defocusing parameter B is proportional to the despace from the paraxial focus position.

Omit the first phase factor (and coefficient) according to the R. Gonsalves' approximation,

$$h(x,y) = \int du \int dv \exp[-2\pi iB(u^2+v^2)]\exp[-2\pi i(ux+vy)]H(u,v) \tag{3.3}$$

This field obeys the following Fresnel diffraction equation

$$-2\pi i \frac{\partial h}{\partial B} = \nabla^2 h \tag{3.4}$$

where $\nabla^2 = \frac{\partial^2}{\partial x^2} + \frac{\partial^2}{\partial y^2}$

and where $h = |h|\exp(i\phi)$ (3.5)

Eq. (3.4) is still valid even without the above Gonsalves approximation, when the distance to the focal plane F is replaced by the variable (z+F), and the defocus parameter B is replaced by BF/(z+F) in Eq. (3.2). The approximation holds for small z compared to F.

The image field equation, which is complex-valued, yields two real-valued image equations, one for the derivative of the intensity with respect to B, and the other for the derivative of the phase with respect to B.

These results apply to any plane, not just the image plane, except where a Fourier transform relationship to the pupil plane is invoked.

FIRST IMAGE PLANE EQUATION

The *first* equation, for conservation of energy, is (generalized Gonsalves case; R. A.Gonsalves, "Phase retrieval by differential intensity measurements," *J. Opt. Soc. Am. A*, **4**, 166-170, 1987; also see K. Ichikawa, A. W. Lohmann, and M. Takeda, "Phase retrieval based on the irradiance transport equation and the Fourier transform method: experiments," *Applied Optics*, **27**, 3433-6, 1988)

$$-\pi \frac{\partial |h|^2}{\partial B} = \nabla \cdot (|h|^2 \nabla \phi) \qquad (3.6)$$

where the right-hand side parentheses contain the energy flux. All *gradient*, *divergence* or *curl* operations are with respect to the variables x and y, and not z. This equation holds generally in any plane, within the Fresnel propagation approximation, when B is replaced by its equivalent that is proportional to the z-variable.

This energy transport equation is obtained from the field equation by separating the real and imaginary parts of the equation after substituting for the field its equivalent magnitude times phase factor. The transport equation comes from the imaginary part, while the second equation, given later, comes from the real part.

The change ΔB in the defocus parameter B is proportional to the amount of defocus Δz.

$$\Delta B = \frac{\lambda}{2} \Delta z \qquad (3.7)$$

A value of defocus distance

$$\Delta z = 8\lambda \frac{F^2}{D^2}$$

yields one wave change at the pupil edge (diameter D). The effective $F_{no.}$ of the telescope and camera system is F/D. This particular length Δz is the spatial period for the spots of Arago on the optical axis.

The *general* form for the image-plane phase, ϕ , is obtained from the flux

$$|h|^2 \nabla\phi = \nabla\psi + \nabla \times A \tag{3.8}$$

in terms of unknown potentials ψ and **A**. Note that *div*(**curl A**) = 0. So that the **curl** part of the flux does not help balance the change in intensity along the z-direction.

The most important step is to solve Poisson's equation for ψ

$$-\pi \frac{\partial |h|^2}{\partial B} = \nabla^2 \psi \tag{3.9}$$

Note that $\nabla^2\psi$ relates to the intensity change axially alone, while $\nabla^2\phi$ relates to the intensity change along a ray, axially, and sideways as well, as given by the direction of $\nabla\psi$.

Let it be noted that without the **curl A** contribution the contours of constant phase are parallel to the contours of constant intensity.

SECOND IMAGE PLANE EQUATION

The *second* equation that obtains from the field equation

$$-2\pi i \frac{\partial h}{\partial B} = \nabla^2 h \tag{3.10}$$

is

$$-\pi \frac{\partial \phi}{\partial B} = \frac{1}{2}|\nabla\phi|^2 - \frac{1}{2|h|}\nabla^2|h| \tag{3.11}$$

the equivalent of the Eikonal equation.

A spatially-varying refractive index term is included customarily.

Because the *unknown* components of the gradient of the phase, in both axial and transverse directions, appear in this equation, there is no application for

this Eikonal equation as such. Of course, the original, simpler Fresnel equation for the complex field would be valid at any point and would be preferable to using Eq. (3.11) anyway.

PHASE RETRIEVAL EQUATION SOLUTION

The left-hand side of the phase retrieval equation is approximated by means of the small differences between two images that are slightly defocused from each other.

$$\frac{\partial |h|^2}{\partial B} = \text{(Pixel-by-Pixel Differences)} / \Delta B$$

The defocus distance, that is, the difference of position Δz is related to the difference in the so-called Goddard position as

$\Delta z = 110 \cdot (1.25)^2$ x Goddard position difference.

For example, Goddard position difference = 5 μm yields Δz = 0.86 mm.

SPECIAL IMAGE PLANE CYCLIC FLOW SOLUTIONS TO ADD

Generally, the contours of constant phase are not parallel to the contours of constant intensity. Aside from trivial differences owing to an overall tilt to the phase wavefront, this difference of contour maps can be attributed to the **curl A** contribution, referred to here as cyclic flow solutions. This is in analogy to the vortex flows in hydrodynamics. Since the $\pm 2\pi$ phase jumps caused by these wavefront dislocations, do not affect the actual values of the fields themselves, the propagation to the near field or the pupil plane is unchanged as well. So the inclusion of these cyclic solutions in the image planes is not necessary for retrieving the phase in the pupil plane. However, these dislocations or vortices occur wherever the intensity is zero. This is especially true of the *exit* pupil plane due to the effect of the obscurations.

The following discussion of the image plane is to better understand these cyclic solutions in general. The same equations for the field amplitude and phase hold for any plane, not just an image plane. And in particular, it is these same cyclic flows, which occur in the *pupil* plane, that are specially treated to yield the underlying smooth wavefront to be approximated by Zernike polynomials, for example.

To represent straight vortex filaments parallel to the optical axis, the vector potential **A** is allowed to have a z-component only, as an approximation. The gradient operator applies here only to the x and y coordinates. Then,

$$\mathbf{A} = a(x,y)\mathbf{e}_z$$

and

$$\nabla \times \mathbf{A} = \nabla a \times \mathbf{e}_z \tag{3.12}$$

and the added phase ϕ_0 is given by

$$|h|^2 \nabla \phi_0 = \nabla a \times \mathbf{e}_z \tag{3.13}$$

$$4\pi\zeta \mathbf{e}_z = \nabla x \nabla \phi_0 = -\mathbf{e}_z \nabla \cdot \frac{\nabla a}{|h|^2} + \mathbf{e}_z \cdot \nabla \frac{\nabla a}{|h|^2}$$

where the vorticity, in a discrete representation, is

$$\zeta = \sum_j q_j \delta^{(2)}(\mathbf{r} - \mathbf{r}_j)$$

upon allowing negligible variation in the z direction. This is an allowance that should be reexamined in the light of the focal plane in the classic case of the circular aperture discussed later. But for now, one obtains

$$\nabla \cdot \frac{\nabla a}{|h|^2} = 0 \tag{3.14}$$

except at points $\mathbf{r}_j$ where the intensity $|h|^2$ vanishes. At these nulls the right-hand side of Eq. (3.14) is proportional to a delta function such that integrating over it yields a $\pm 2\pi$ change ($q_j = \pm 1$). Let

$$\nabla \chi = \frac{\nabla a}{|h|^2} \quad .$$

where, because of Eq. (3.14),

$$\nabla^2 \chi = 0 \tag{3.15}$$

The contours of constant a or χ are parallel to those of constant intensity or ψ. Laplace's equation is solved with the boundary condition that the circulation singularity strength be $+2\pi$ or -2π wherever the intensity has a simple zero. These singularities are wavefront dislocations (like vortex filaments or sheets). With an explicit z dependence reintroduced, these vortex filaments and sheets may close upon themselves in a three-dimensional manner. This matter is pursued further in the section on special solutions.

Thus,

$\chi = \ln|h| + \ldots$

where the additional non-singular term (denoted by the ellipses) is another function of \h\ that allows χ to satisfy Laplace's Eq. (3.15) with the appropriate geometrical boundary conditions, and to follow the contours of constant intensity.

The phase contribution ϕ_0 is given by

$$\nabla^2 \phi_0 = 0 \tag{3.16}$$

where ϕ_0 is the imaginary part of the analytic function (in a region avoiding the dislocations and made singly-connected by branch cuts), whose real part is χ.

These considerations of phase dislocations and vortex filaments apply to any plane, not just the image plane. In particular, the pupil plane phase has several dislocations, which are locally averaged out (in the Roddiers' POLE routine described later) to yield the desired smooth Zernike polynomial representation of the wavefront error and, hence, the primary mirror deformation.

APPROXIMATE SOLUTION FOR IMAGE PLANE PHASE

Solve for the phase from

$$\nabla \phi = \frac{\nabla \psi}{|h|^2} + \nabla \chi \times \mathbf{e}_z \tag{3.17}$$

Note the mathematical identity that

$$\nabla \cdot \nabla \chi \times \mathbf{e}_z = 0$$

Then, the phase is

$$\phi = \nabla^{-2} \nabla \cdot \left(\frac{\nabla \psi}{|h|^2}\right) + \phi_0 \tag{3.18}$$

where

$$\nabla \psi = -\pi \nabla^{-2} \nabla \frac{\partial |h|^2}{\partial B} \tag{3.19}$$

The operations of inverse Laplacian ∇^{-2} and so on are easily implemented in Fourier space, or in the case of cylindrical symmetry, in appropriate radial-coordinate integration.

When ϕ_0 is *un*important, phase contours are parallel to intensity contours. Phase contours are sensitive to details of log (intensity).

The contours of constant ϕ_0 are perpendicular to the contours of constant intensity, in this approximation. The intensity contours are like streamlines to the flow, which is given by the gradient of this added phase. This is cyclic flow around the zero intensity points and confined by the intensity contours.

With the phase ϕ determined, perform the Fourier transform of

$$|h|\exp(i\phi)$$

Obtain

$$H = |H|\exp(i\Phi) \tag{3.20}$$

Then, obtain the exit pupil phase Φ. Basically, this is the phase to be retrieved.

When the corresponding phase is obtained for the unaberrated case, that phase can be subtracted from this exit pupil phase to obtain the contribution due to the aberration itself. The amplitudes can be corrected also.

SPECIAL VORTEX SOLUTION

The classic case of the field distribution due to an illuminated circular aperture shows that the z-dependence of the **A** potential can be abrupt, contrary to the assumptions so far. The vortex filaments consist of a set of infinitesimally thin concentric rings, which lie in the focal plane alone and which encircle the optical axis. These lie at the locations of the Airy dark rings. Meanwhile, on axis are infinitesimal vortex rings, similar to dipoles or doublets, that lie at the periodic minima, the dark spots of Arago. Between these are the more famous bright spots. All these vortices, i.e., the rings and the doublets, are special because they have no extension in the z-direction.

With a finite frequency spread and with the axial uniform flow superposed, some of the streamlines of energy flux circulate around these vortex rings if they are very nearby to any part of a vortex ring. But much of this flow goes by without making the trip around. There is a surface which divides the circulating flow from the noncirculating flow for each vortex ring. There are stagnation points for

the flow on these dividing surfaces. These points are intensity maxima, the Airy rings and Arago spots. See Fig. 3.1 for a sketch of this vortex ring configuration for the focal region for a uniformly illuminated circular aperture.

The rings have circulation all in the same sense of rotation around the axis, while the doublets have their rotation all together in the opposite sense. This sums to zero total angular momentum.

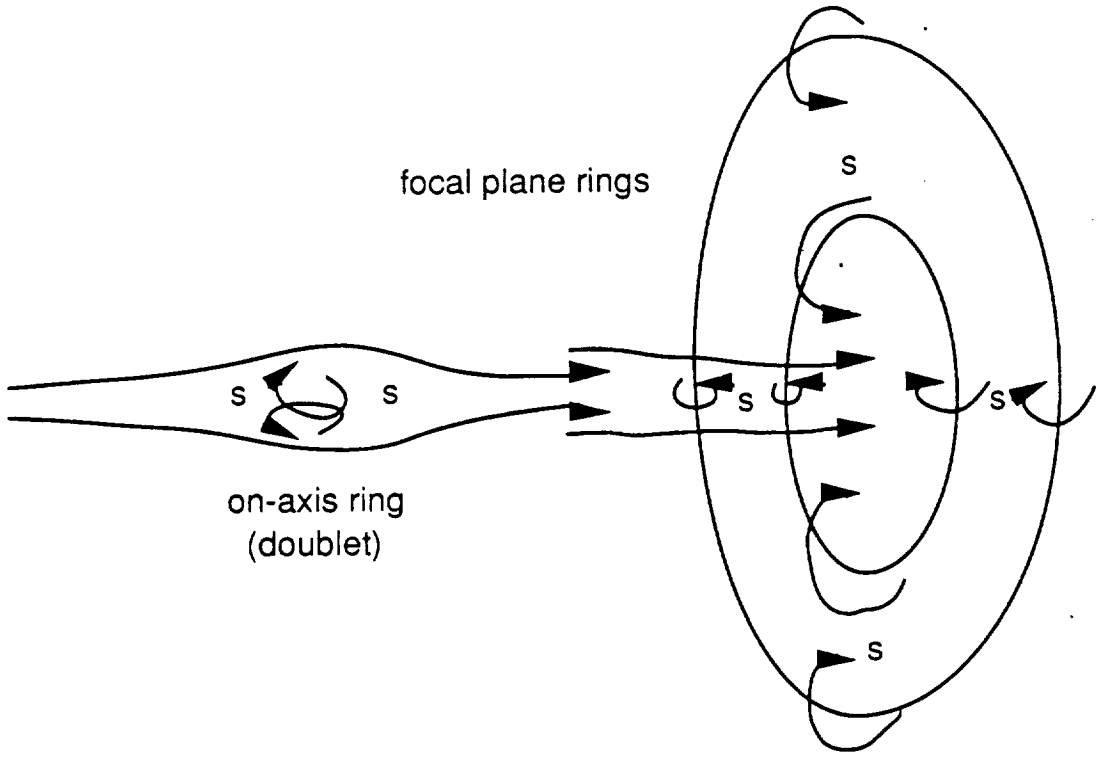

Fig. 3.1. Schematic of the streamlines of photon flow around the focal plane vortex rings (only two are shown) corresponding to the Airy dark rings and the whirls associated with one of the on-axis rings, corresponding to a dark spots of Arago. The stagnation points in the flow are denoted by s, where the bright spots or bright rings are located. The whirls are actually distributed uniformly around the circumference of each of their underlying rings. The geometrical focus is at the center of the Airy rings. Only parts of the nearly horizontal streamlines are shown.

The width of the circulatory regions that surround each vortex ring depends on the frequency bandwidth of the light, according to J. F. Nye and M. V. Berry, *Proc. R. Soc. Lond.* A. **336**, 165-190 (1974). Their Fig. 10 shows an enlarged drawing of the region in the immediate vicinity of a vortex filament. A section of a vortex ring would resemble a vortex filament. Their Fig. 10 is oriented at 90 degrees to Fig. 3.1. The intensity nulls, where the vorticity lies, can be thought of as caused by interference between the wavelets that diffract from the edges of the circular aperture, and by the interference at the focal plane between the shrinking cylindrical wave in front of the focal plane and the expanding cylindrical wave behind the focal plane.

In *Principles of Optics*, 6th ed.,Pergamon Press, Oxford, 1980, pp. 445-6, M. Born and E. Wolf describe the phase distributions in the focal region. In their Figs. 8.45 and 8.46, the little open circles denote these nulls. These are also the cross-sections of the vortex rings in the focal plane. Fig. 8.45 also shows the on-axis ring, which is infinitesimal in diameter and equivalent to a doublet, as in fluid dynamics. The ray paths shown above in Fig. 3.1, run perpendicular to the co-phasal surfaces plotted by Born and Wolf in their two Figs.

Baranova *et al.* (*Sov. Phys. JETP* ,**53**(5), 925-929, May 1981 and *J. Opt. Soc. Am.* **73**(5), 525-528, May 1983) discuss the vortex filaments, *i.e.*, the wavefront dislocations that extend in the direction of the optical axis (z axis). Noisy wavefields cause speckle patterns and cause creation and annihilation of filamentary dislocations in pairs of opposite sign. The intensity is zero on these filaments.

The treatment of the vortex filaments in Eqs. (3.12-3.17) could be generalized by allowing the *gradient*, *divergence* , *curl* and Laplacian operators to include the partial derivative with respect to z, too. The original energy transport equation would include the contribution from the divergence of the flux component in the z direction as well. The three-dimensional Laplace's equation for phase ϕ_0 would be solved, except for the singularities where the intensity is zero. The vector potential **A** would lie nearly parallel to the vorticity, which exists only where the intensity is zero, *i.e*, in a direction perpendicular to both the gradient of the intensity and to the gradient of this phase. Earlier this vorticity was introduced as a two dimensional delta function with a coefficient such that this phase will change by $\pm 2\pi$ around a filament (whether straight or bent around in a ring). More generally, the filaments can be treated as three-dimensional configurations carrying this unit of strength.

Then, the desired cyclic solution of Poisson's equation is obtained from

$$\nabla \phi_0(\boldsymbol{\rho}) = \nabla \times \int \frac{d^3\boldsymbol{\rho}'}{|\boldsymbol{\rho}' - \boldsymbol{\rho}|} \zeta(\boldsymbol{\rho}') \tag{3.21}$$

(Biot-Savart law) for a general vorticity geometry. The position vector $\boldsymbol{\rho}$ (and $\boldsymbol{\rho}'$) is in curvilinear coordinates, two of which lie within surfaces of constant intensity and the third is perpendicular to them.

This phase ϕ_0 reduces to the solid angle subtended by a simple closed three-dimensional circuit of vorticity. The solid angle jumps by 4π upon passing through the circuit. This causes an apparent discrepancy by a factor of two when comparing the two- and three- dimensional cases, i.e., linear angle around a length of filament *vs.* solid angle when passing through a closed circuit.

When dealing with thin filaments along the z-axis (ζ-axis), as in the earlier discussion for the two-dimensional case, Eqs. (3.14)-(3.17), the analytic function

$$\chi(\rho) = \int \frac{d\zeta' d^2\rho_\perp'}{|\rho' - \rho|} \sum_j q_j \delta^{(2)}(\rho_\perp' - \rho_{\perp j}) \cong \sum_j q_j \ln|\rho_\perp - \rho_{\perp j}| \qquad (3.22)$$

where the vorticity is given a discrete representation at the prescribed points denoted by the two-dimensional $\rho_{\perp j}$. These points include all boundaries of the aperture and obscured regions, where the intensity is zero and where filament *images* might be used instead of boundary conditions on the vorticity. This is necessary to achieve parallel contours of intensity and of χ, or orthogonal contours with respect to ϕ_0. The coordinates in Eqs. (3.21) and (3.22) are orthogonal to contours of constant intensity.

Based on the approximation in Eq. (3.22), the corresponding analytic function for the cyclic phase is

$$\phi_0(\mathbf{r}_\perp) \cong \sum_j q_j \arg(\rho_\perp - \rho_{\perp j})$$

A conformal transformation from $\rho_\perp$ to $\mathbf{r}_\perp$ completes the specification of the cyclic solution.

3.2 Image Interpolation

The width of the mathematical square aperture in the pupil plane exceeds the diameter of the primary mirror by a factor, $n_a \lambda/\lambda_0$, which allows interpolation between the grid points that represent the pixels when a Fourier transform to the image plane is performed. This factor corresponds to increasing the resolution by exactly n_a, which equals two or four, for example, independent of the filter wavelength. The reference wavelength, λ_0 , is 0.508 μm (15.24μm / $F_{no.}$) for the OTA/PC combination, whose effective $F_{no.} = 30$.

The intensity at each pixel is now shared by the n_a x n_a pixels. These are weighted according to relative intensities in a model calculation for images from the aberrated OTA. The amount of aberration used here is given by the equivalent of a conic-constant error that is typical of present knowledge about the error. The distance of the image planes from the paraxial focus position is an important parameter for the model calculation.

The image field is cropped, usually by a factor of two reduction. This is to avoid aliasing when Fourier transforming back to the pupil planes. Aliasing, which is due to undersampling, is the undesirable overlay of data from the apparently equivalent periodic regions that arise from the assumption of sine and cosine Fourier representations of the data.

3.3 Phase Unwrapping

The pupil phase is obtained from the arctan(ImH/ReH), where the argument of the arctan function is the ratio of the imaginary and real parts of the field H. This

phase lies between $-\pi$ and π, by definition of arctangent. The continuous phase distribution is obtained from this generally discontinuous distribution by the subroutine POLE that was obtained from the Roddiers (as reported at the Image Inversion Workshop).

The method of unwrapping the phase is to add or subtract 2π from the original phase distribution at appropriate places. An elementary loop is formed by the four adjacent pixels of each grid square of the pupil plane. Each phase difference that corresponds to a side of each loop is checked to see if it exceeds in magnitude the value π. If so, then the appropriate 2π is subtracted or added to reduce each such phase difference to less than π in magnitude. The new phase differences are then summed around each such loop. Each sum, in turn, is checked for zero value. If not zero then the center of the offending loop, called a pole, is assigned a $+2\pi$ or a -2π value, as appropriate to the sense of *circulation*. Note that discontinuities of phase by the amount π can still exist. These corresponds to a phase change by going half way around a vortex filament. These filaments are taken to be of unit strength, i.e., $\pm 2\pi$, and not integer multiples because such multiple filaments are believed to be unstable to splitting into unit-strength filaments (B. Ya. Zel'dovich, *et al.* in *Principles of Phase Conjugation*, Springer-Verlag, Berlin, 1985, pp. 79-84).

These poles are joined by straight lines (one line per pole) into closest pairs of opposites in sign of circulation. Excess poles are joined to the nearest boundary points of the aperture. The line joining such a pair of poles is called a dislocation by the Roddiers. This is the branch cut for the multivalued phase function. The vortex filaments themselves might better be called dislocations, like the screw dislocations of solids.

The poles themselves are like vortices for the vector field formed by the phase differences. As many as hundreds of poles are found in the retrieved phase distribution, without using the averaging over azimuthal angle. With the averaging, the number of poles drops to tens, for example. These poles may have extension in the axial direction to form vortex filaments. Then, the Roddier branch cuts would form sheets.

The phase distribution is obtained by summing the original phase differences along horizontal rows (working from the bottom upward) until a dislocation is encountered. Then, the appropriate jump of $\pm 2\pi$ is applied in the vertical direction across the dislocation. At the end of this phase unwrapping the pixels on the dislocations themselves are given the average values of their nearest non-dislocation pixels. This last step removes any vestiges of curl contributions in the pupil plane phase map.

3.4 End-to-End Wave Optics Model

The exit pupil phase contains the effects of the optical train even when free of aberrations. To determine the effect of the aberrations alone, the ideal phase should be subtracted from the retrieved phase, and the ideal pupil amplitude divided into the retrieved amplitude. Furthermore, the defocusing operation on

HST is done by displacement of the secondary mirror, which displacement introduces additional aberrations besides defocusing that are modeled as well.

A calculation of the ideal phase and amplitude properties was done by Fresnel propagation along the OTA and PC axes. This follows the Code V prescription provided by JPL. An efficient Fourier transform technique is used to implement the propagation from element to element in the train, in the presence of large changes in magnification. This was related to the Talanov transformation, according to S. Ebstein, and used by the Roddiers in their repeated Fresnel transform (double Fourier transform) technique, as described at the first HARP Image Inversion Workshop.

The mirror surfaces for OTA and PC are modeled by appropriate conics of revolution (hyperboloids). The field flattener lens is modeled as a simple paraboloid (quadratic phase factor) lens and spacer.

Test runs have shown the image at the focus of the OTA, namely, at the pyramid, to be about as expected. However, the image produced at the image plane of the PC was not like observed images. The propagation algorithm through the PC was very similar to that for the OTA. The nature of the difficulty was not clear.

While the end-to-end model was being debugged, phase retrieval test and interpolation results were obtained using a primary and a camera mask for specifying the input of relative intensities, i.e.,the zeros and ones of the two pupil functions. For the simple simulations and interpolations, these two masks were merely multiplied together and input at the primary mirror. However, the end-to-end model has the PC6 mask input at the relay (camera) primary (or somewhat upbeam), while the OTA mask was input at the OTA primary. These masks consist of the near-central obscurations, the spider-support obscurations, and, for the OTA, the three low-reflecting mounting pads. The PC6-channel orientation of these elements was considered only.

3.5 Zernike Polynomial Fitting

The pupil plane wavefront phase map was expressed as a sum of polynomials, chosen to be the orthogonal set of Zernike type with a 0.33 fractional radius for a central obscuration. The first 22 of these were tabulated in the HST OTA Handbook, vers. 1.0, May 1990. These were normalized to unity integral over the clear aperture area, and, hence, unit *rms* value.

The least-squares routine obtained the coefficients of the polynomial expansion by fitting the phase factor, the exponential function of i times the phase, rather than the phase function itself. In part, this circumvents the ambiguities of multiples of full waves. However, phase unwrapping was done to remove these ambiguities anyway.

The error metric that is to be minimized is

$$\text{Error} = \sum \left| \exp(i\Phi_k) - \exp(i\Theta_k) \right|^2 |H_k|^2 \; / \; \sum |H_k|^2 \qquad (3.23)$$

where Φ_k is the digital data to be fit and Θ_k is the sum of Zernike polynomials. The subscript k denotes data at points x_K within the annular aperture. The quantity H_k is the retrieved pupil field distribution. The sum with respect to the subscript k in the denominator is the total power within the annular aperture.

$$\Theta_k = \sum a_M Z_M(x_k) \qquad (3.24)$$

The normal equations for minimization are used to solve for the increments Δa_M in the polynomial coefficients.

$$\frac{\partial \text{Error}}{\partial a_M} = -2 \sum \sin(\Phi_k - \Theta_k) Z_M(x_k)$$

$$\frac{\partial^2 \text{Error}}{\partial a_M \partial a_N} = 2 \sum \cos(\Phi_k - \Theta_k) Z_M(x_k) Z_N(x_k)$$

$$\Delta a_M = -\sum \left[\frac{\partial^2 \text{Error}}{\partial \mathbf{a} \partial \mathbf{a}} \right]^{-1}_{MN} \frac{\partial \text{Error}}{\partial a_N} \qquad (3.25)$$

The matrix element is the MN *th* element of the inverse matrix of second derivatives of the error metric. Sums are over the repeated index on the various quantities on any of the right-hand sides.

These equations are nonlinear. During an iteration procedure they depend on the previous values of the polynomial coefficients. Schemes for improving convergence of the iterations that are performed in this minimization routine are straightforward but untried here. Without the smoothing effect of phase unwrapping this simple iteration procedure is usually unstable.

3.6 Error Estimates for Phase Retrieval

Noise Effects

By means of a reverse Strehl ratio calculation, i.e., averaging over the image plane instead of the pupil plane, and by the *Cumulant* Theorem (see M. Abramowitz and I. A. Stegun, *Handbook of Mathematical Functions*, U.S. Gov't, Wash.,DC, 1972, p. 928 (item 26.1.12); and R. Kubo, "A Stochastic Theory of Line Shape and Relaxation," in *Fluctuation, Relaxation and Resonance in Magnetic Systems*, ed. D. Ter Haar, Plenum, NY, 1962, pp. 23-68) on exponential functions, the variance of the pupil plane phase (in radians) is obtained from

$$\langle \exp(i\delta\Phi)\rangle \cong \exp(i\langle\delta\Phi\rangle - \frac{1}{2}\langle\delta\Phi^2\rangle)$$

$$= \langle \exp(\delta \ln|h| + i\delta\phi)\rangle \cong \exp(i\langle\delta \ln|h|\delta\phi\rangle + \frac{1}{2}[\langle(\delta \ln|h|)^2\rangle - \langle\delta\phi^2\rangle]) \qquad (3.26)$$

where the usual factor $\exp\langle \ln|h|\rangle$ was included in the definition of the averaging in order to create the aperture function by Fourier transform, and was not included as part of the contribution to the phase. The imaginary-valued cross-correlation term contributes to the average pupil phase.

Then,

$$\langle\delta\Phi^2\rangle \cong -\frac{1}{4}\langle(\delta \ln|h|^2)^2\rangle + \langle\delta\phi^2\rangle \qquad (3.27)$$

$\langle\ \rangle$ denotes the spatial weighted-average over *image* area, instead of over the usual pupil area for the usual Strehl ratio. The δ denotes the statistical deviation due to noise or other random effects. Specifically,

$$\langle \exp(i\delta\Phi)\rangle = \frac{\int d^2r \exp(-2\pi i\mathbf{u}\cdot\mathbf{r})h_0(\mathbf{r})\exp(\delta \ln|h| + i\delta\phi)}{\int d^2r \exp(-2\pi i\mathbf{u}\cdot\mathbf{r})h_0(\mathbf{r})} \qquad (3.28)$$

where

$$\langle f(\delta \ln|h|, \delta\phi)\rangle = \frac{\int d^2r \exp(-2\pi i\mathbf{u}\cdot\mathbf{r})h_0(\mathbf{r})f(\delta \ln|h|, \delta\phi)}{\int d^2r \exp(-2\pi i\mathbf{u}\cdot\mathbf{r})h_0(\mathbf{r})}$$

for any function f of the fluctuations. The underlying image field h_0 produces the aperture function by Fourier transform.

It is simple and reasonable to assume that the statistical probability distribution is Log-Normal for image intensity and Normal, i.e., Gaussian, for image phase.

The subtractive term on the right-hand side of Eq. (3.27) will be smaller than the second term on the right-hand side, according to the estimates below, and as required by the positivity of the left-hand side of that equation.

The fluctuation in logarithm is related to the small noise fluctuation by

$$\delta \ln|h|^2 \cong \ln(\text{signal} + \text{noise}) - \langle \ln(\text{signal} + \text{noise}) \rangle$$

$$\cong \delta\text{noise} / (\text{signal} + \langle \text{noise} \rangle)$$

so that, for example,

$$\left\langle (\delta \ln|h|^2)^2 \right\rangle \cong \frac{1}{(1+\text{SNR})^2} \tag{3.29}$$

for a simple exponential noise probability distribution over the image area, for which

$$\left\langle \delta\text{noise}^2 \right\rangle = \langle \text{noise} \rangle^2$$

SNR denotes the signal-to-noise ratio for area-averaged quantities. This does not refer to temporal statistics at a given pixel, which are close to Poisson statistics, for which

$$\left\langle \delta\text{noise}^2 \right\rangle = \langle \text{noise} \rangle$$

The Cumulant Theorem was applied , over the image area, to assumed spatial Gaussian statistics for the random variables in the exponents. This simple case, for which the cumulant sum is truncated at the second term, is the limit for any type of statistics when the fluctuations are weak and/or compact. That is, the value of the product of *rms* modulation of spatial gradients of the random variables and correlation distance is smaller than one. If the correlation distance is only on the order of a pixel or two, then the *rms* gradient of ln(intensity) need be small over that distance.

But with the more relevant Poisson noise statistics over the image area, in terms of numbers of noise equivalent-photoelectrons and signal photoelectrons per *image*, Eq. (3.29) becomes

$$\left\langle (\delta \ln|h|^2)^2 \right\rangle \cong \frac{\langle \text{noise} \rangle}{(\text{signal} + \langle \text{noise} \rangle)^2} = \frac{\langle \text{noise} \rangle^{-1}}{(1+\text{SNR})^2} \tag{3.30}$$

SNR of greater than tens are found for the cropped images, while at least a few hundred noise equivalent-photoelectrons per pixel would be found. About 128 x 128 pixels are used per image.

The image phase, ϕ, excludes tilt and focus terms, in effect, because of the Fourier transform phase term: $-2\pi \mathbf{u}\cdot\mathbf{r}$, which is implicitly included. The quantity $\mathbf{u}$ is the pupil plane position, in spatial frequency or in spatial pupil-plane position divided by λF, at which the variance of the phase Φ is being estimated.

With no central obscuration, this would be at the center of the pupil plane corresponding to **u=0**, in the spirit of a Strehl ratio. However, the variance in Eq. (3.27) is evaluated at a typical point in the clear aperture, where the aperture function is unity.

An estimate of the phase error is obtained by way of the phase retrieval equation, Eq. (3.18), when a simplification is made that the term involving the gradient of the reciprocal intensity can be neglected. This is explained as follows:

In the absence of dislocations, near an intensity maximum,

$$\phi = \nabla^{-2}\nabla \cdot \left(\frac{\nabla\psi}{|h|^2}\right)$$

where

$$\nabla\psi = -\pi\nabla^{-2}\nabla\frac{\partial|h|^2}{\partial B}$$

Note that

$$\nabla^2 = \frac{1}{r}\frac{\partial}{\partial r}r\frac{\partial}{\partial r} + \frac{\partial^2}{r^2\partial\theta^2}$$

for the two-dimensional case dealt with here. For angle-independent quantities,

$$\nabla^{-2} = \int_0^r \frac{dr'}{r'}\int_0^{r'} dr''r'' \tag{3.31}$$

where the lower limits of integration were chosen to eliminate logarithm and constant terms.

Upon making use of the operator identity

$$\nabla \cdot \nabla^{-2}\nabla = 1$$

which follows from interchanging the order in which partial derivatives are done,

$$\nabla^{-2}\nabla = \nabla\nabla^{-2}$$

and from using the definition of the Laplacian operator

$$\nabla \cdot \nabla = \nabla^2$$

and, for the sake of simplicity, upon neglecting the gradient of the reciprocal intensity near an intensity maximum, where the gradient vanishes, the retrieved phase is approximately

$$\phi \cong -\pi\nabla^{-2}\frac{1}{|h|^2}\nabla\cdot\nabla^{-2}\nabla\frac{\partial|h|^2}{\partial B} = -\pi\nabla^{-2}\frac{1}{|h|^2}\frac{\partial|h|^2}{\partial B}$$

or

$$\phi \cong -\pi\nabla^{-2}\frac{\partial \ln|h|^2}{\partial B} \tag{3.32}$$

Then, with the finite difference approximation to the derivative with respect to the amount of defocus between the two image planes

$$\frac{\partial \ln|h|^2}{\partial B} \cong \frac{\Delta \ln|h|^2}{\Delta B}$$

and with the variance of this quantity

$$\left\langle\left(\delta\left(\frac{\partial \ln|h|^2}{\partial B}\right)\right)^2\right\rangle \cong \frac{\left\langle(\delta\Delta \ln|h|^2)^2\right\rangle}{(\Delta B)^2} \cong \frac{2\left\langle(\delta \ln|h|^2)^2\right\rangle}{(\Delta B)^2}$$

and, with the variance of $\nabla^{-2}\ln|h|^2$

given by

$$\left\langle\left(\delta\nabla^{-2}\ln|h|^2\right)^2\right\rangle \cong \left\langle\left(\int_0^r\frac{dr'}{r'}\int_0^{r'}dr''r''\int_0^{2\pi}\frac{d\theta}{2\pi}\frac{\delta n(\mathbf{r}'')}{s+n}\right)^2\right\rangle$$

$$\cong \left\langle\left(\int\frac{d^2r''}{2\pi}\ln(r/r'')\frac{\delta n(\mathbf{r}'')}{s+n}\right)^2\right\rangle$$

$$\cong \int\frac{d^2r'}{2\pi}\ln(r_0/r')\int\frac{d^2r''}{2\pi}\ln(r_0/r'')\left\langle\frac{\delta n(\mathbf{r}')}{s+n}\frac{\delta n(\mathbf{r}'')}{s+n}\right\rangle$$

$$\cong \frac{\pi r_0^2}{2(2\pi)^2} \frac{\langle (\delta n)^2 \rangle d_{pixel}^2}{(s+n)^2} \cong \frac{\pi r_0^2 d_{pixel}^2}{2(2\pi)^2 (1+SNR)^2 \langle noise \rangle}$$

then

$$\langle \delta\phi^2 \rangle \cong \left\langle \left(\pi \nabla^{-2} \delta \frac{\partial \ln|h|^2}{\partial B} \right)^2 \right\rangle$$

$$\cong \left[\frac{\lambda_0^2}{\lambda^2} \frac{\lambda F_{no.}^2}{\Delta z} \frac{1}{1+SNR} \right]^2 \frac{1}{n_{pixel}} \qquad (3.33)$$

where Δz is the defocus distance, and $\pi r_0^2 = N_0^2 d_{pixel}^2$,where r_0 is the radius of the image region. N_0^2 is the number of pixels utilized per image. There is an extra factor of two in the numerator because the variance is of the difference of two fluctuating $\ln|h|^2$ quantities in $\Delta \ln|h|^2$. The δ denotes deviations from the appropriate spatial mean. The pixel size $d_{pixel} = \lambda_0 F_{no.}$ Note that the subtractive term in Eq. (3.27) can be ignored when relating Eq. (3.33) to the *pupil* phase variance.

Slipping the angular brackets inside the integrals is done by an appropriate interchange of the order of integrations. The statistical approximation for the noise correlation function

$$\langle \delta n(\mathbf{r}') \delta n(\mathbf{r}'') \rangle \cong \langle (\delta n(\mathbf{r}'))^2 \rangle d_{pixel}^2 \delta^{(2)}(\mathbf{r}' - \mathbf{r}'') \qquad (3.34)$$

was used. This is equivalent to treating the noise in the different pixels as statistically independent of each other. This whole procedure is somewhat cavalier, but useful for a rough estimate of the variance.

The average signal density per unit area was denoted by s and the average noise areal density by n. That is,

$$n = \langle noise \rangle / (\pi r_0^2)$$

Note that the noise per pixel is

$$n_{pixel} = \langle noise \rangle / N_0^2$$

This phase error is *inversely* proportional to $(1+\mathrm{SNR})\sqrt{n_{pixel}}$ With SNR between 10 and 100, with λ =0.959 λ_0 at 487 nm, with N_0 = 128, and with $\Delta z = 2 \lambda F_{no.}^2$, as is the case for these data, the rms phase error is between 0.01 and 0.001 waves, respectively, when there are a typical 100 equivalent noise photoelectrons per pixel, a convenient reference level.

Defocus Error

Other sources of error might dominate this noise error. The so-called breathing in and out of the focal position is such a case, especially if the characteristic time is comparable to the data integration time, while the amplitude of the effect is comparable to the separation distance of the pair of image planes used for phase retrieval. There is no indication for such a difficulty from these results.

Shorter exposure images, with the narrower central peaks, were dealt with first. These would be less affected by the breathing defocus action and also less by alignment jitter.

If the error in the image plane separation Δz is important, then

$$\left\langle \delta\phi^2 \right\rangle \equiv \left\langle \left(\pi \nabla^{-2} \delta \frac{\partial \ln|h|^2}{\partial B} \right)^2 \right\rangle$$

$$\equiv \left\langle \left(\pi \int_0^r \frac{dr'}{r'} \int_0^{r'} dr'' r'' \int_0^{2\pi} \frac{d\theta}{2\pi} \frac{\partial^2 \ln|h|^2}{\partial B^2} \delta(\Delta B) \right)^2 \right\rangle \qquad (3.35)$$

Here the angular brackets denote averaging over the ensemble of fluctuations in the defocus distance.

For simplicity in evaluating the second derivative, the image intensity is temporarily assumed Gaussian-shaped, having width that fits to the diffraction from a uniformly-filled aperture and that has blurring due to defocusing a distance z from paraxial focus. The blurring due to spherical aberration is deferred from consideration for the moment.

$$\ln|h|^2 \equiv \ln|h_0|^2 - \frac{\left(\frac{\pi r}{2\lambda F_{no.}} \right)^2}{1+w^2} + \ldots$$

and

$$\frac{\partial^2 \ln|h|^2}{\partial B^2} \cong 2\frac{w^2}{B^2}\frac{3w^2-1}{(1+w^2)^3}\left(\frac{\pi r}{2\lambda F_{no.}^2}\right)^2 \qquad (3.36)$$

where

$$w = \frac{\pi B}{8\lambda^2 F_{no.}^2} = \frac{\pi z}{16\lambda F_{no.}^2}$$

Then

$$\sqrt{\langle \delta\phi^2 \rangle} \cong \left(\frac{\partial^2 \ln|h|^2}{\partial B^2}\frac{\pi r^2}{16}\right)\sqrt{\langle [\delta(\Delta B)]^2 \rangle} \qquad (3.37)$$

Note that the *rms* error increases with the *fourth* power of the radius in the image, when the quadratic dependence in the second derivative is included.

A fractional error $\delta(\Delta B)/\Delta B$ of 10 percent (say, 0.5 μm out of 5 μm in Goddard units) yields $\delta(\Delta z) = 0.0086$ cm. When $z = -1.96$ cm (at -114 Goddard units) and the quantity for blurring $w = -8.8$, then an *rms* phase error of 0.04 waves is estimated at the edge of the image. If the variance is averaged over the image area, the final *rms* error relevant to the pupil phase is a factor 2.236 smaller. Then, the pupil phase error is approximately 0.018 waves.

These are only rough estimates, while errors in ΔB are not yet known. There is no strong evidence that the breathing motion of focus jitter has greatly affected the difference quantity ΔB in the measurements at 487 nm that were used here.

Other Errors

The quantity B itself is to be measured from the paraxial focus position, which is a parameter that is varied as part of the least squares fitting to Zernike polynomials.

Another error source has been the unwrapping of the phase, where the pupil wavefront dislocations are smoothed over, in a final step. The full two-dimensional Fourier method of phase retrieval yields a wavefront with many dislocations. Zernike polynomial fits to these smooth unwrapped phase distributions seemed consistently shifted from the corresponding fits to the azimuthally-averaged (one-dimensional) phase distributions. This shift has not been made quantitative yet, due to the limited number of runs in the two-dimensional case, and due to the wider polynomial set allowed for this case.

The Zernike fitting introduces errors due to a dependence on the number of polynomials that are allowed in the set to be fit, even in the simple cylindrically

symmetric case. When the HST OTA Handbook Z_{22} polynomial (fifth order spherical aberration) is included along with the usual Z_1 (piston), Z_4 (focus) and Z_{11} (third order spherical aberration), a limiter on the amount of change in coefficient for Z_{22} at each iteration sometimes has to be introduced to prevent numerical instability. Apparently, there is some underlying interdependency of the variables that makes the inverse matrix elements small when involving this last polynomial.

Error due to digitization with 12 bits has not been a difficulty. The dynamic range of 0 to 4095 seems adequate to handle the large central peak of the point spread function. Saturation effects on the images have been avoided by choosing those image pairs with the narrower central peaks.

Shot noise and read-out noise were the main contributors to the noise in the signal-to-noise ratio estimated to be between 10 and 100.

Flat-fielding error and errors due to cosmic-ray spike removal were not evaluated. These were not expected to contribute more than the shot noise in the image central region that contributed most significantly to this phase retrieval.

4.0 Major Findings

4.1 Task Results

4.1.1 Task 1. HST Point Source Images

Digital data of point source images were obtained from the JPL VAX facility via magnetic tape and SPAN in September. The data were of the same source at different wavelengths and at different focal positions. The focal position was changed aboard HST by movement of the OTA secondary mirror. Attention was mainly directed to the data set designated PC6F487N_G1.FITS, ...H1...,...I1..., and ...G2...,...H2...,...I2.... These data correspond to narrow band 487-nm signal with the OTA secondary mirror at the Goddard positions of -5, 0 and 5 μm. This early choice was made on the basis of proximity of the positions to the 'best' focus, and the small despace between images.

Digital data of point source images were obtained from the JPL VAX facility via magnetic tape in November. The data were of the same source at different wavelengths and at different focal positions. Attention was directed to the data set designated PCF487N_O1&2.FITS and PCF487N_P1&2.FITS. These data correspond to narrow band 487-nm signal with the OTA secondary mirror at the Goddard positions of -267 and -260 μm. At these same Goddard positions, but with narrow band 889-nm signal, the set PCF889N_O1 &P1.FITS was also analyzed. These choices were made on the basis of small despace between images, while representing cases of severe blurring.

The images appear to require no additional registration within the image frames for centering the images on each other.

4.1.2 Task 2. Phase Retrieval Code

The phase retrieval code was implemented on other simple test cases. Large arrays (256 X 256) were used to reduce the raggedness of the circular edges on the numerical grid. Effects of filtering out high spatial frequencies in the pupil phase function was explored. Flat phase to less than 0.06 waves was retrieved for the input flat phase case with the centrally-obscured circular aperture.

The phase retrieval code was modified to deal with a cylindrically-symmetric average of the data. The differential equation of this direct phase retrieval technique is now integrated in the radial coordinate in the image plane. This substitutes for the Fourier transform equation-solving technique used for the general case.

The rings of zero intensity in the image plane caused half-wave phase jumps. These are dealt with more accurately in the cylindrically-symmetric, non-Fourier equation-solving case. These zeros arose from the hard edges of the apertures in the near-field. The reconstruction of the pupil plane amplitude and phase would better show the obscuration characteristics of telescope and camera when the half-wave phase jumps are calculated better in the image plane

phase distribution. However, an accurate reproduction of the pupil plane characteristics would require the full two-dimensional phase retrieval technique.

The energy transport equation for the cylindrically-symmetric case is

$$-\pi\frac{\partial I}{\partial B}=\frac{\partial}{r\partial r}[rI(r,B)\frac{\partial\phi}{\partial r}] \qquad (4.1)$$

where I(r,B) is the image intensity distribution (averaged over azimuthal angle) in the plane, whose axial coordinate is proportional to the defocus parameter B.

This equation is integrated to solve for the phase in the image plane.

$$\phi=-\pi\int_0^r dr'\frac{1}{r'I(r',B)}\int_0^{r'}dr''r''\frac{\partial I(r'',B)}{\partial B} \qquad (4.2)$$

This solution has the boundary conditions built in that the phase is zero at the center and that its slope is also zero there.

Note the division by the intensity within the last integration. The zeros of intensity, as discussed before, lead to half-wave jumps in phase. In principle, these jumps would result from the integration. However, in practice the values of intensity in the vicinity of each zero are known only very roughly on the image plane grid. The intensity values are small near the zeros and introduce errors in the result. For reasons that involve reintroducing terms that were dropped in the paraxial or Fresnel approximation right at the beginning, this denominator was replaced by the following more accurate and less offending quantity:

$$\sqrt{a^2+b^2}$$

where the original denominator

$$a=r'I(r',B)$$

and the new contribution

$$b=-\pi\int_0^{r'}dr''\frac{\partial I(r'',B)}{k\partial B}r''$$

where $k=2\pi/\lambda$.

The quantities *a* and *b* are proportional to the components of the local ray direction. This follows from a good approximation that the rays lie on the surface of constant enclosed power, which is the area integral of the intensity up to a radius *r*. It follows from the energy transport equation that while the

curvature of the rays is slight so that $\nabla^2\phi \cong 0$ as in incompressible flow, (the Laplacian now includes the second order z-derivative), and while the rays are still mainly parallel to the z-axis and the intensity changes are mainly radial, the slope of a ray is approximately

$$\frac{dr}{dz} = -\frac{\partial P / \partial z}{\partial P / \partial r} \qquad (4.3)$$

where the enclosed power P is

$$P = 2\pi \int_0^r dr' r' I(r', z) \qquad (4.4)$$

Note that z and B are proportional. Note also, that exactly at a vortex position, the quantity *b*, as well as *a*, is zero, whereby the ray direction is indeterminate.

However, with this modified denominator, the phase ϕ is correctly given by the ray path integral along the radial direction, with the appropriate sine of the angle of this ray with respect to the axis, instead of the tangent of this angle. The two trigonometric functions are usually nearly equal, except where the intensity is small, and where the dominance of the axial wave vector component is no longer a good approximation. Nevertheless, the new integrand is now *bounded*, since the sine, in magnitude, is less than or equal to one.

A similar revision of the denominator in the two-dimensional phase retrieval algorithm was introduced.

The wave optics propagation routine for dealing with the different planes containing obscurations, apertures and other optical elements of the OTA and the PC was developed. Details of the pads and spiders were introduced for the OTA and the PC models. The secondary mirror position can be changed to cause defocusing of the image. The aberrations introduced by this change can be modeled with this code, as well as providing test images for phase retrieval and for interpolation between the pixels of actual data.

As an instructive exercise, the prescription, provided by JPL, for the HST OTA and the PC, was entered into Code V at TRW. Various plots were made to clarify the configuration.

Appropriate geometrical specifications were introduced into the wave optics code to nearly complete the end-to-end propagation capability that this code would provide.The strategy to distinguish the phase aberration contributions of the OTA primary from those of the secondary mirror would depend on this code, when used for cases of different incident field angles for the star images. Also, besides changing the focal position, motion of the secondary mirror produces small aberrations to the wavefront.

4.1.3 Task 3. Preliminary Wavefront Characteristics

The test cases indicated that the polynomial fitting was sensitive to even very small effects such as the rapidly varying intensity and phase conditions at or near the pupil edge, and the discrete square grid of input data that impressed a four-fold symmetry on the retrieved phase.

The even-simpler test case of uniform phase (i.e., no spherical aberration) over a circular aperture, with a circular central obscuration (like the OTA case), revealed similar four-fold symmetry features, even for the 256 X 256 element pupil-grid case.

The (second) iterative fitting scheme outlined by J. R. Fienup (HARP Image Inversion Workshop, Nov. 1990) was implemented to decrease sensitivity to phase unwrapping. However, the normal equations for minimization were used to supply the changes in coefficients for the next iterations.

The Goddard position for paraxial focus was varied from case to case until a best fit was obtained according to the least residual error. The interpolation between pixels was redone for each of these cases.

The phase unwrapping routine of C. and F. Roddier, discussed briefly at the November HARP Workshop, was implemented. The routine has run, where hundreds of wavefront jumps (dislocations) were unwrapped and smoothed for the Fourier, two-dimensional phase retrieval technique, while only tens of dislocations arose and were handled in the cylindrically-averaged version of the phase retrieval.

4.2 Separating Primary and Secondary Aberration Contributions

The strategy for separating the contributions from the three sources: the primary mirror, the secondary mirror and the camera, was still being formulated. The fact that the phase contributions would be weighted differently with changes of field angle would be critical.

The geometrical optics limit would yield the resultant OTA phase as the sum of the phase contributions from primary and secondary mirrors along any given ray path between them, and then on to the image. Wave optics alone would make a very small, angle-dependent, correction to this sum.

$$h(\mathbf{r}) = \int \frac{d^2K}{(2\pi)^2} f_p(\mathbf{K}) f_{ps}(\mathbf{K} - \Delta\mathbf{K}) f_s([\mathbf{K} + \Delta\mathbf{K} - \frac{k\mathbf{r}}{F}]M) \qquad (4.5)$$

where **K** is the Fourier transform wavevector variable in the two-dimensional integral, k is the usual $2\pi/\lambda$, $\Delta\mathbf{K}$ is the wavevector corresponding to the off-axis field angle, M is the secondary magnification (based on the secondary's illuminated diameter), and F is the effective focal length of OTA

$$f_p(\mathbf{K}) = F.T.[\exp(i\Delta\Phi_p)]$$

is the coherent point spread function for the OTA primary, where $\Delta\Phi_p$ is the phase deviation from paraboloid shape of the primary.

$$f_{ps}(\mathbf{K}) = M\exp[-iK^2Md/2k]$$

is the wave propagator between primary and secondary (distance apart, d).

$$f_s(\mathbf{K}) = F.T.[\exp(i\Delta\Phi_s)]$$

is the coherent PSF for the OTA secondary, where $\Delta\Phi_s$ is the phase aberration of the secondary. F.T. denotes Fourier transform operation.

In the geometrical optics limit: $f_{ps}(\mathbf{K}) = M$ so that

$$h(\mathbf{r}) \cong M\int \frac{d^2K}{(2\pi)^2} f_p(\mathbf{K}) f_s([\mathbf{K} + \Delta\mathbf{K} - \frac{k\mathbf{r}}{F}]M)$$

$$= F.T.[\exp(i\Delta\Phi_p + i\Delta\Phi_s)] \qquad (4.6)$$

where $\Delta\Phi_p + \Delta\Phi_s$ is evaluated at points on the same ray that goes from primary to secondary mirror and onward.

The small correction for wave optics is obtained by Taylor expanding the propagator f_{ps}.

$$\Delta h(\mathbf{r}) \cong M\int \frac{d^2K}{(2\pi)^2} f_p(\mathbf{K})(-i|\mathbf{K} - \Delta\mathbf{K}|^2Md/2k) f_s([\mathbf{K} + \Delta\mathbf{K} - \frac{k\mathbf{r}}{F}]M) \qquad (4.7)$$

This correction term is inversely proportional to the Fresnel number of the secondary mirror, owing to the fact that the typical spatial frequencies associated with **K** are only of the order of the reciprocal diameter of the primary. The two magnification factors lead to a Fresnel number based on the diameter of the secondary. This Fresnel number is very large, so that the effect of wave optics, compared to geometric optics is small in this case.

The important point is that the sum of phases, primary plus secondary, is different for different angles of input wavefront tilt, given by $\Delta\mathbf{K}$. If the contribution from the primary is nearly the same then the change in the sum is

mainly due to the secondary. Thus, data for different off-axis objects would yield the required information on the secondary mirror.

This procedure was not attempted, however. Effects of the images lying near a corner of the CCD chip rather than near the center, and other effects, needed to be evaluated first.

4.3 Conic-Constant Error

The relationship between the Zernike spherical aberration coefficient Z_{11} (μm) and $\Delta K'$ the error in conic constant is related to the fourth-order dependence on ρ, the fractional radial distance in the pupil plane. For the spherical aberration coefficient, the optical path difference (in meters) due to the mirror deformation is

$$OPD = \Delta K' \, r \, \rho^4/(8 \, R^3) = 0.5 \, Z_{11} \, 10^{-6} \, 16.896 \, \rho^4 \qquad (4.8)$$

where r = 1.2 m, the radius of the primary mirror, and R = (11.04 m)/(1.2 m), the ratio of the radius of curvature to the mirror radius. The factor of 0.5 converts wavefront phase to mirror deformation. The factor 16.896 provides the correct spherical-aberration polynomial normalization, with a 0.33 obscuration ratio, so that over the clear aperture, the area integral of the square of the polynomial is unity. Then, the coefficient is the *rms* value of spherical aberration over this clear aperture annulus.

Values for Z_{11} at the wavelengths 0.487 and 0.889 μm were -0.27 and -0.28 μm. The reason for the discrepancy is not known. These two wavelength cases were from HARP 1A and 1B data, respectively. A similar difference of Z_{11} has been noted by R. Lyons (at the second HARP workshop) for these data sets, irrespective of wavelength.

At 487 nm, the Zernike polynomial coefficients (0.33 obscuration ratio) in waves, for piston, focus, third order and fifth order spherical aberration, with the paraxial focus distance at -114.0±0.02 Goddard units, were

based on H1-I1 data:
$Z_1 = -3.69 \pm 0.01$, $Z_4 = -2.95 \pm 0.01$, $Z_{11} = -0.560 \pm 0.002$, $Z_{22} = 0.0378 \pm 0.002$;

based on G1-H1 data:
$Z_1 = -3.59 \pm 0.02$, $Z_4 = -2.85 \pm 0.01$, $Z_{11} = -0.553 \pm 0.003$, $Z_{22} = 0.0006 \pm 0.003$.

Compare these with
$Z_1 = -3.54$, $Z_4 = -2.70$, $Z_{11} = -0.560$, $Z_{22} = 0.0$,
for a pure quartic:
-0.273 μm $16.896 \, \rho^4$
for the effect of conic constant error. Note that Z_{22} should be negligible (of order 10^{-4}) for the actual (hyperboloid) conic figure of revolution. The first factor in the coefficient of ρ^4 is the derived Z_{11} in waves times the wavelength in μm.

At 889 nm, the Zernike coefficients in waves, with paraxial focus distance at the later observation date approximately equal to -119±1 Goddard units, were

Based on O1-P1 data:
Z_1 = -2.15±0.01, Z_4 = -1.64±0.01, Z_{11} = -0.319±0.005, Z_{22} = -0.0951±0.0003.

Compare with
Z_1 = -2.01, Z_4 = -1.54, Z_{11} = -0.319, Z_{22} = 0.0,
for a pure quartic:
-0.284 μm 16.896 ρ^4
for the effect of conic constant error. Again, the first factor in the coefficient of ρ^4 is the derived Z_{11} times the wavelength in μm.

5.0 Conclusions

The retrieval results indicated sensitivity of the fitting of Zernike coefficients to symmetry anomalies in the data, such as the four-fold symmetry due to the square grid of pixel intensity data. The data, when averaged over angle in the image plane, and the direct integration technique, using only the radial coordinate, helped to overcome this difficulty.

The phase unwrapping (full-wave jump smoothing) routine of the Roddiers handled the fragmented phase that was retrieved, especially when the input to the retrieval was image data that was averaged over angle around the central pixel.

The derived Zernike coefficients depended on the paraxial focus position chosen. However, when the Goddard position of the paraxial focus was varied as a parameter, a definite best fit was found. This was characterized by a significantly lower residual error than found at neighboring values of paraxial focus positions. The paraxial focus was, thus, found to be -114.0 μm for the HARP 1A 487-nm data. The results for the HARP 1B 889-nm data were less definitive with respect to low residual error, owing to the much more blurred images and owing to some constraint needed on the Z_{22} coefficient during fitting.

The Zernike coefficient Z_{11} (HST OTA Handbook) was -0.27 and -0.28 μm for the H1-I1 and O1-P1 pairs of images, at 487 and 889 nm, respectively. By using the formula obtained from the previous OPD relation,

$$\Delta K' = Z_{11}/22.802 \qquad (5.1)$$

the error offset in conic constant is -0.0118 and -0.0123. The *rms* error in the Zernike coefficient was ±0.005. This was estimated from the standard deviation for fitting (converged iterations) of the polynomial coefficients at 889 nm, associated with a narrow range of paraxial focus distances (-119±1). The error due to polynomial fitting in the 487 nm data was somewhat less.

The design conic constant was -1.0022985. Then, the estimated conic constant is -1.0141 for the 487-nm HARP 1A data and -1.0146 for the 889-nm HARP 1B data, with *rms* error of ±0.0002 due to polynomial fitting.

Acknowledgment. Thanks are given for the encouragement and criticism by R. Korechoff and A. Vaughan, for the helpful comments by J. Trauger, M. Shao, M. Colavita, E. Granger, A. Meinel, J. Fienup, S. Ebstein, and R. Gonsalves, for the HARP newsletter by K. Leschley, for the data magnetic tapes by R. Evans and coworkers, for the VAX-related advice by C. Lowry, and especially for the routines obtained from and discussions with C. and F. Roddier. Discussions with and support by J. Thomson, A. Schnurr and D. O'Keefe are greatly appreciated.